The Astrophysical Journal, 657:559–566, 2007 March 1

ARE ALL CORONAL MASS EJECTIONS HOLLOW FLUX ROPES?

J. Krall
Plasma Physics Division, Naval Research Laboratory, Washington, DC
Received 2006 August 16; accepted 2006 October 12

ABSTRACT

A quantitative specification of a three-dimensional flux rope is examined statistically for comparison to previously published statistical measures of coronal mass ejections (CMEs) as observed by the *Solar Maximum Mission* (*SMM*) spacecraft. The three-dimensional geometry that has been previously shown to reproduce statistical measures (average angular widths) of CME image data that show flux-rope morphologies is based on a "hollow" pre-eruption density structure extrapolated into the corona. It is shown that the *SMM* results are consistent with this hollow flux-rope geometry.

Subject heading: Sun: coronal mass ejections (CMEs)

1. INTRODUCTION

Interplanetary coronal mass ejections (ICMEs) are well established as significant drivers of space weather (Gosling 1993; Bothmer & Schwenn 1995; Gonzalez et al. 1999; Marubashi 2000). Because the magnetic structure of an ICME appears to be closely related to that of its near-Sun counterpart (coronal mass ejection or CME; Bothmer & Schwenn 1994; Yurchyshyn et al. 2001, 2006; Bothmer 2003; Rust et al. 2005; Krall et al. 2006), the three-dimensional structure of CMEs is a topic of great interest.

In a recent study, Krall & St. Cyr (2006) determined the quantitative parameters of a "typical flux-rope CME." In that work, a typical flux-rope CME was defined to be a three-dimensional flux-rope geometry that reproduced specific quantitative results of a statistical study (St. Cyr et al. 2004) of flux-rope-like CME images from the Large Angle Spectrometric Coronagraph (LASCO; Brueckner et al. 1995). Specifically, an ensemble of synthetic coronagraph images was generated for the given geometry by considering an array of possible orientation angles, only some of which produced synthetic images with the flux-rope morphological features of interest. In that study, relevant CME image data were limited to those images showing both a three-part structure and a well-defined leading-edge feature that encompasses the CME and appears to remain connected to the Sun. Additional necessary features included, for so-called broadside events, an overarching looplike structure and, for so-called axial events, a concave-outward tailing-edge feature along with multiple concentric curved features between the leading and trailing edges. Because both the synthetic and the actual coronagraph images used in that study were limited to those that showed these specific morphological features, the resulting three-dimensional flux-rope geometry, shown in Figure 1, is applicable only to "flux-rope CMEs." Let us now ask if this same flux-rope CME geometry can reproduce quantitative observational results for a complete population of CMEs (not just the ones that look like flux ropes). If it can, then the result would support the conjecture that all CMEs are flux ropes and that those that appear to be either axial or broadside views of a flux-rope magnetic structure are merely the subset of all CMEs that are viewed advantageously.

Other studies of CME morphology and geometry (Cremades & Bothmer 2004, 2005; Howard et al. 2005) are generally consistent with a flux-rope geometry with footpoints remaining connected to the Sun, at least while the CME leading edge is within 6 $R_\odot$ of Sun center, as discussed here. The graduated cylindrical shell used by Howard et al. (2005) is an example of a hollow flux-rope configuration featuring more parameters than that of Krall & St. Cyr (2006). Howard et al. (2005) demonstrated model-fits to four specific events, selected from among a set of "structured CMEs" identified by Cremades & Bothmer (2004). However, they did not fit enough events to determine average parameters for the underlying CME geometry. In each of these studies (St. Cyr et al. 2004; Cremades & Bothmer 2004, 2005; Howard et al. 2005; Krall & St. Cyr 2006), measured CME populations were limited to those that met specific morphological criteria.

The specific aim of this paper is to examine the hypothesis that most, if not all, observed CMEs are consistent with an underlying flux-rope structure similar to that determined by Krall & St. Cyr (2006) and shown in Figure 1. In particular, if most CMEs are flux ropes and if this flux-rope geometry indeed represents an average CME flux rope, then it should be possible to use this geometry to reproduce statistical results obtained by measuring a general population of CME events. Whereas Krall & St. Cyr (2006) limited their study to images (both actual and synthetic) that showed flux-rope morphologies, this new study encompasses more general populations of CME images and corresponding ensembles of synthetic images.

In this effort, CME statistics from two published studies of the *Solar Maximum Mission* (*SMM*; Strong et al. 1999) CME data are used. Statistical measures from a study of 111 *SMM* limb events (Burkepile et al. 2004) are considered, as well as results from two studies of much larger sets of *SMM* CME events that are not restricted by source location (Webb et al. 2003; Burkepile et al. 2004).

For example, Burkepile et al. (2004) considered 111 *SMM* limb CMEs, which were defined to be events that had associated eruptive prominence (EP) or flare-source activity within 15° of the solar limb. The CME population in this case has a known distribution of position-angle latitudes, which is closely related to the distribution of latitude angles, but can be assumed to be uniformly distributed in the other two orientation angles that we use (a longitude angle and a tilt about the direction of motion), within the restriction that the source longitude lie within 15° of the limb. Burkepile et al. (2004) found that the mean apparent width for this sample was $52.3^\circ \pm 2.2^\circ$ and that the median width was 46°. If the specific geometry of Krall & St. Cyr (2006) is typical of all CME events, then a corresponding ensemble of synthetic CME images should come close to reproducing these mean and median angular widths. In all cases, ensembles of CME images

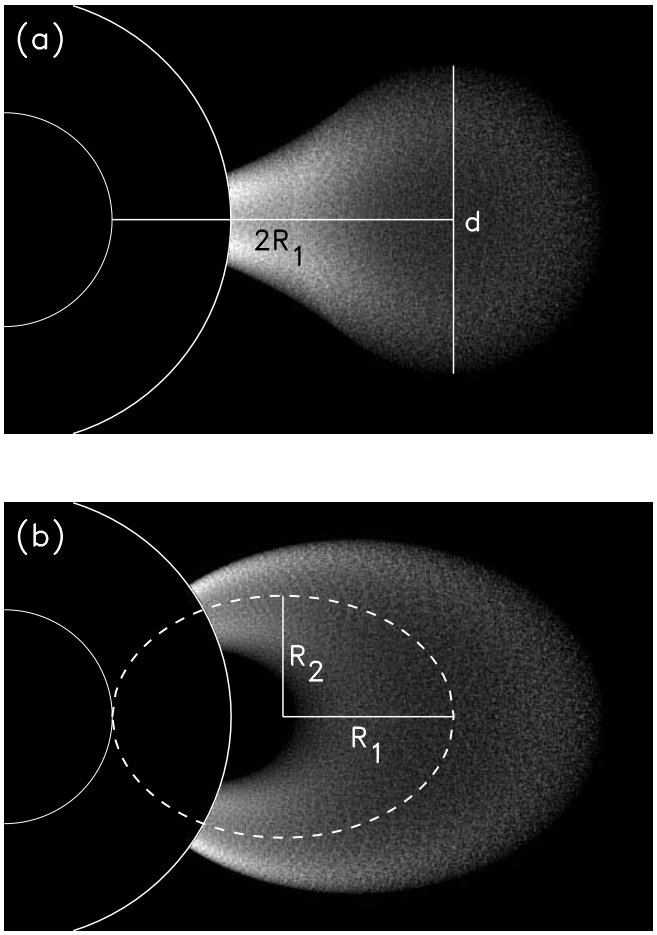

FIG. 1.—Synthetic coronagraph images of a parameterized flux rope showing (*a*) axial and (*b*) broadside views. Here, $\epsilon = 0.70$ and $\Lambda_a = 1.1$.

shall be generated by considering a distribution of orientation angles that approximates that of the CME data (to the degree that this is known) but with a fixed geometry.

In the Webb et al. (2003) study, the occurrence of concave-outward features, such as those illustrated in the synthetic coronagraph image of Figure 1*a*, is reported for *SMM* CME events. Concave-outward features within CMEs can occur if the density structure of the CME corresponds to that of a hollow flux rope; that is, a flux rope in which the on-axis density is reduced significantly relative to the density near the edge of the flux rope (Chen et al. 2000). Indeed, this density structure and the resulting morphological features are key elements of the Krall & St. Cyr (2006) study. Examples shown in Chen et al. (2000), Krall & Chen (2005), and Krall & St. Cyr (2006) illustrate and quantify this density structure, with the center-to-edge density ratio ranging from 4 to 7. The latter value, used in Krall & St. Cyr (2006) and again here, is based on a determination of the density structure of a pre-eruption solar flux rope by Krall & Chen (2005) that was extrapolated into the corona (Krall & St. Cyr 2006). Of course, these flux ropes are not hollow in the sense that the low-density region contains relatively high magnetic fields (Gibson & Low 1998; Krall & Chen 2005). Just as we focus on statistical measures of the CME geometry in comparing an ensemble of synthetic CME images to the results of Burkepile et al. (2004), we focus on the hollow nature of the flux rope by comparing our results to those of Webb et al. (2003). Thus, the frequency of occurrence of concave-outward features, similar to those discussed in Webb et al. (2003), are considered for the specific geometry of Krall & St. Cyr (2006) via an ensemble of synthetic coronagraph images corresponding to an appropriate distribution of orientation angles.

The comparisons, presented below, between the results obtained using the fixed flux-rope geometry of Krall & St. Cyr (2006) and those obtained from *SMM* observations represent a test of the Krall & St. Cyr (2006) result against a broader set of observations than was previously used. Here the aim is not to obtain a new best-fit flux-rope geometry but instead to test the hypothesis that the previous result is applicable to a general population of CMEs. Nevertheless, the sensitivity of the results to the flux-rope geometric parameters is also examined.

The flux-rope parameterization and the statistical procedure are discussed in §§ 2 and 3 below. Results appear in §§ 4–6, followed by conclusions in § 7.

2. CME PARAMETERIZATION

As was done in Krall & St. Cyr (2006), the flux rope is described as having a curved axis and, at each point along the axis, a circular cross section. In keeping with the observations, the width (minor diameter) is narrowest at the foot points on the solar surface and thickest at the apex, where the width is d. Generally in keeping with the observations, but also to simplify the parameterization, it is again assumed that the curved axis of the flux rope traces out an ellipse.

This is illustrated in Figure 1, which shows synthetic coronagraphs of exactly axial and exactly broadside views of the flux-rope geometry of Krall & St. Cyr (2006) corresponding to two views of a flux-rope CME with the apex moving radially outward from the west limb. In Figure 1*b* it is shown that the axis of the parameterized flux rope traces out an ellipse, which is referred to as the flux-rope ellipse.

The flux rope is parameterized in terms of the eccentricity $\epsilon = [1 - (R_2/R_1)^2]^{1/2}$ of the flux-rope ellipse and the axial aspect ratio $\Lambda_a = 2R_1/d$, the ratio of major diameter of the flux-rope ellipse to the apex diameter d. In Krall & St. Cyr (2006) it was found that a typical flux-rope CME has an eccentricity $\epsilon = 0.7 \pm 0.2$ and an axial aspect ratio $\Lambda_a = 1.1 \pm 0.3$. Throughout most of this study, fixed values $\epsilon = 0.7$ and $\Lambda_a = 1.1$ are used, as shown in Figure 1.

It is important to point out that the above is a quantitative description of CME geometry rather than CME morphology. The latter can be obtained from measurements of CME images, as was done by St. Cyr et al. (2004) and Cremades & Bothmer (2005). For example, St. Cyr et al. (2004) found that in images of flux-rope CMEs the ratio of the average broadside width to the average axial width was $78^\circ/48^\circ = 1.6$. In a similar study, Cremades & Bothmer (2005) found a roughly equivalent ratio of 1.6. Krall & St. Cyr (2006) showed that, with projection effects accounted for, the St. Cyr et al. (2004) morphological result is consistent with an underlying geometry in which the ratio of exactly broadside to exactly axial angular widths is 1.9 (see Krall & St. Cyr 2006, § 5), as shown in Figure 1.

3. PROCEDURE

In this study, synthetic coronagraph images are used to make the connection between the underlying geometry and measurable aspects of actual CME images (see Appendix A of Krall & St. Cyr [2006] for details on the generation of synthetic coronagraph images of a parameterized flux rope; see also Chen et al. 2000). This is done in order to obtain results for comparison to observations. In each observational result of interest, a set of CME images is considered based on specific selection criteria. Statistical results are then generated by, for example, measuring the angular width of the CME in each image and reporting mean

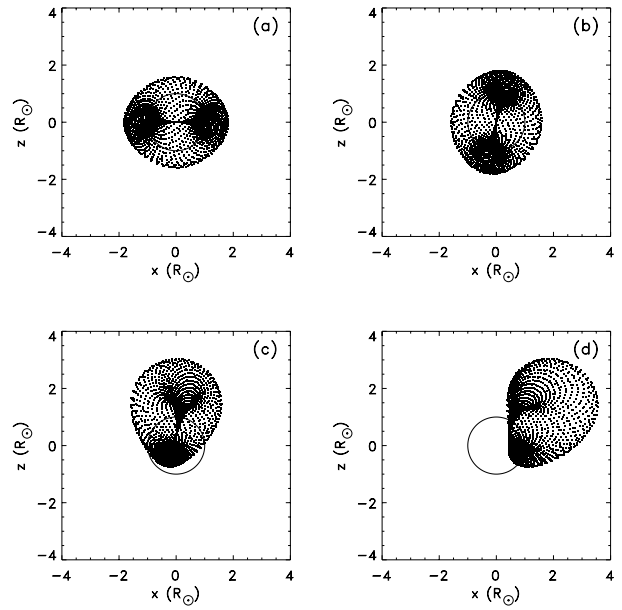

FIG. 2.—Plots projecting the shape of the outer surface of the flux-rope geometry onto the plane of the sky, with various orientation angles: (*a*) all angles set equal to zero; (*b*) same as (*a*), but with $\alpha_y = -79^\circ$; (*c*) same as (*b*), but with $\lambda_0 = 19^\circ$; (*d*) same as (*c*), but with $\phi_0 = 28^\circ$.

and median values for the entire set. To obtain the synthetic results in each case, an ensemble of flux-rope orientation angles is considered consistent with the observational selection criteria while holding the geometry constant. In each case, two ensembles are being compared. In the observed ensemble there is a distribution of orientation angles and of geometric parameters. In the numerically generated ensemble, the distribution of orientation angles is approximately the same as in the observations, and the (unknown) actual distribution of geometries is replaced by a single fixed geometry. In the event that this fixed geometry is truly a typical CME geometry, it is assumed that these two ensembles are approximately equivalent in the sense that a sequence of measurements at a fixed position is equivalent to an ensemble of possible states at a fixed time for a stationary ergodic ensemble (Reif 1965).

Consistent with the measurements of Webb et al. (2003) and Burkepile et al. (2004), all synthetic coronagraph images are computed so as to be comparable to the *SMM* coronagraph with an "occulting disk" of radius 1.6 $R_\odot$. Also consistent with these *SMM* results, the projected (morphological) position of the CME leading edge is at the same specified height above Sun center, 4.0 $R_\odot$, in all synthetic images.

The orientation angles to be varied are the tilt of the flux rope about the axis defined by the direction of motion (α_y), the source latitude (λ_0), and the source longitude (ϕ_0). For the purpose of orienting the flux rope, a coordinate system is defined with its origin at Sun center, the *z*-axis upward, the *x*-axis directed toward the west limb, and the *y*-axis directed along the Earth-Sun line, away from the Earth. When orienting the flux rope, one begins with the flux-rope ellipse in the plane of the ecliptic, situated so that one end of the major axis of the ellipse (the "footpoints") sits on the solar surface at disk center. The flux rope extends outward from that point as would be the case for a front-side halo CME. One applies the tilt angle α_y (a rotation about *y*), then moves the source location to the correct latitude λ_0 (a rotation about *x*), and finally moves the source to the correct longitude (a rotation about *z*). This is illustrated in Figure 2, where the flux rope is shown as a set of tracer particles scattered across its outer surface. In Figure 2*a*, all angles are set to zero. In Figure 2*b*, the tilt angle α_y has been rotated to $\alpha_y = -79^\circ$. Figure 2*c* repeats Figure 2*b* but with the latitude angle rotated to $\lambda_0 = 19^\circ$. Figure 2*d* repeats Figure 2*c* but with the longitude angle rotated to $\phi_0 = 28^\circ$. When the result is imaged as a synthetic coronagraph image, the result appears as in Figure 7*a* further below. To provide further examples, we note that $\alpha_y = 0^\circ$, $\lambda_0 = 0^\circ$, and $\phi_0 = 90^\circ$ corresponds to a west-limb event at the solar equator, viewed exactly axially, as in Figure 1*a*, and $\alpha_y = \pm 90^\circ$, $\lambda_0 = 0^\circ$, and $\phi_0 = 90^\circ$ corresponds to Figure 1*b*.

Certain approximations concerning flux-rope CME dynamics are implied above. Specifically, by considering fixed values for ϵ and Λ_a over a range of apex heights above the solar surface, self-similar expansion of the flux-rope geometry is assumed (a range of apex heights results from the range of specified orientation angles at a fixed projected leading-edge height). Previous modeling efforts (Chen et al. 1997; Krall et al. 2001, 2006) show that this is a reasonable approximation. In addition, this specification of the orientation angles describes only cases in which the flux-rope apex moves radially outwards from the chosen latitude and longitude. Where appropriate, the possibility of nonradial motion will be accounted for by considering a range of orientation latitudes and/or longitudes that is greater than the range of observed source-region locations. Based on Webb et al. (2000), Cremades & Bothmer (2004), Krall et al. (2006), and Yurchyshyn et al. (2006), it is assumed that deviations from radial motion (such as a deflection) of 10° are common.

4. COMPARISON TO STATISTICAL MEASURES OF *SMM* LIMB CME EVENTS

Burkepile et al. (2004) considered 111 *SMM* CMEs in which there was associated EP or flare-source activity within 15° of the solar limb. The CME population in this case has a known distribution of apparent position-angle latitudes (see their Fig. 3) centered approximately on the equator, with an rms value of 27°. Burkepile et al. (2004) found that the average apparent angular width for this sample was $52.3^\circ \pm 2.2^\circ$ and that the median width was 46°. Here the reported uncertainty is the standard deviation in the distribution of angular widths divided by the square root of the sample size.

Let us now consider a distribution of specified orientation angles that is approximately consistent with the observed CME population. Because the source region is restricted to being within ±15° of the limb, while the degree of nonradial motion (such as a deflection) is unknown, 10° is added to account for typical nonradial motions so that the source-longitude range is increased to ±25° of the limb. Consistent with Figure 3 of Burkepile et al. (2004), the source-latitude range lies within 50° of the equator. That is, we show a posteriori that we have reproduced, very roughly, the observed distribution of apparent latitudes. Because the tilt angle is unknown, a full range is allowed. To avoid redundant images in the computed ensemble, latitude and longitude angles are limited to the intersection of the northern, western, and Earthward solar hemispheres.

The latitudes used here are $\lambda_0 = 6^\circ$, 19°, 31°, and 44°, which are evenly spaced between 0 and 50°; the longitudes are $\phi_0 =$ 69°, 78°, and 86°, which are evenly spaced between 65° and 90°; and the tilt angles are $\alpha_y = -79^\circ$, -56°, -34°, -11°, 11°, 34°, 56°, and 79°, which are evenly spaced within the range $90^\circ \leq \alpha_y \leq -90^\circ$. For simplicity, the angular distribution of flux ropes will be assumed to be uniform within the chosen ranges. The full set of orientation angles provides an ensemble of 96 synthetic coronagraph images, each generated with a projected leading-edge height of 4.0 $R_\odot$. For example, images obtained for $\lambda_0 = 31^\circ$, $\phi_0 = 78^\circ$, and with the full range of tilt angles are shown in Figure 3.

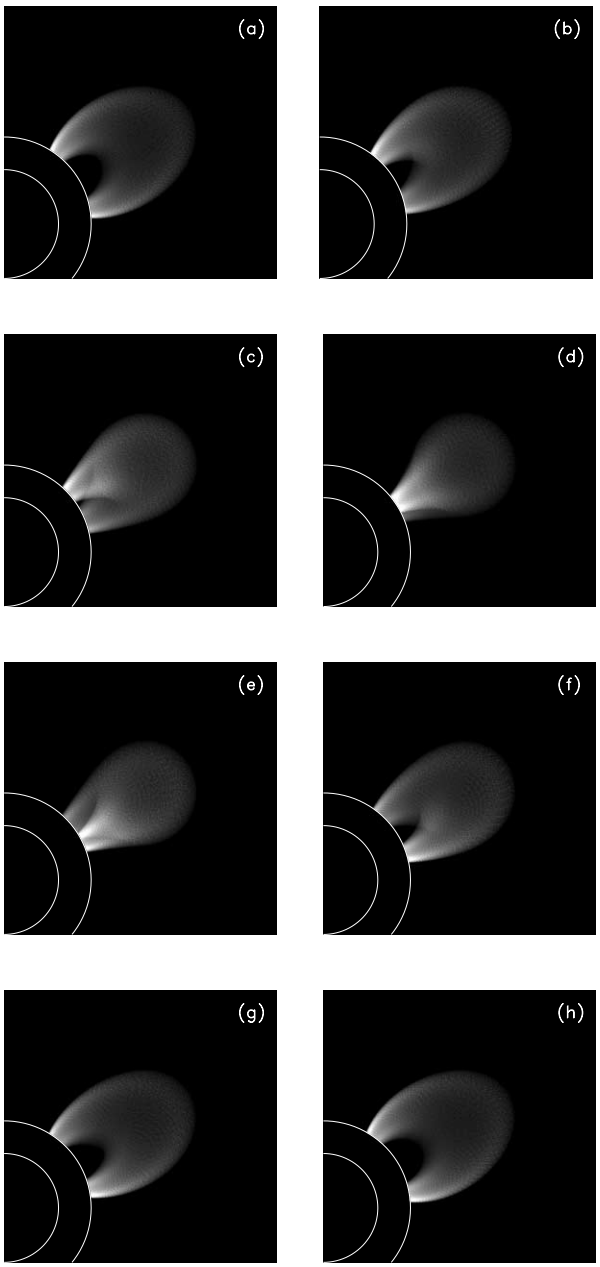

FIG. 3.—Synthetic coronagraph images corresponding to $\lambda_0 = 31^\circ$ and $\phi_0 = 78^\circ$, with (*a*) $\alpha_y = -79^\circ$, (*b*) $\alpha_y = -56^\circ$, (*c*) $\alpha_y = -34^\circ$, (*d*) $\alpha_y = -11^\circ$, (*e*) $\alpha_y = 11^\circ$, (*f*) $\alpha_y = 34^\circ$, (*g*) $\alpha_y = 56^\circ$, and (*h*) $\alpha_y = 79^\circ$. The computed angular widths for images (*a*)–(*h*) are 56.1°, 49.2°, 39.7°, 36.6°, 37.4°, 45.4°, 53.8°, and 57.7°, respectively. Their apparent latitudes are 31.4°, 30.9°, 31.3°, 31.9°, 32.1°, 32.9°, 32.7°, and 32.1°.

The average angular width for the ensemble of 96 images is $47.5^\circ \pm 0.8^\circ$ and the median is 49°. Here, as in Burkepile et al. (2004), the reported uncertainty is the standard deviation in the distribution of angular widths divided by the square root of the sample size. For comparison to the observed distribution shown in Figure 3 of Burkepile et al. (2004), the synthetic distributions of angular widths and apparent latitudes are shown in Figure 4.

The synthetic results for the angular extent distribution are close to those from the observed distribution, with the mean and median differing by only 9% and 6%, respectively. Comparison of Figure 4 to Figure 3 of Burkepile et al. (2004) shows that an angular extent distribution that is generated by considering a distribution of orientations for a single geometry is not equivalent to the observed distribution, which presumably represents a variety

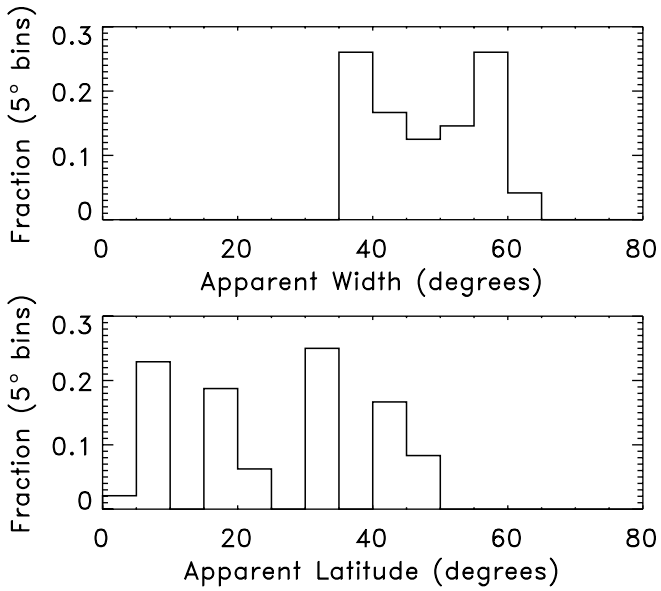

FIG. 4.—Distribution of apparent angular widths (*top*) and apparent latitudes (*bottom*) generated from a single model geometry with varying orientations for source locations near the limb.

of geometries. Because the observed angular-extent distribution includes a "tail" that is not in the synthetic distribution, the relative sizes of median and mean are affected. That the synthetic result reflects a single geometry instead of a spectrum of geometries clearly affects the standard deviation, which is 8.2° in the synthetic angular-extent distribution and 23° in the observed distribution.

This study shows that significant characteristics of the observed distribution of angular widths, specifically the mean and the median, can be approximately reproduced by considering a single specified geometry with a variety of orientation angles. It does not show, however, that allowing variations on that geometry (various values of ϵ and Λ_a) will reproduce the overall shape of the distribution; that is beyond the scope of this study. Indeed, in order to construct a straightforward test of the hypothesis that virtually all CMEs are flux ropes with the typical geometry being that of Krall & St. Cyr (2006), this study was restricted to a single geometry and a very simple (flat) distribution of orientation angles. As a check on the distribution of orientation angles, the apparent latitude was computed in each case in order to find the standard deviation in those values. This rms value is 29° for the synthetic distribution and is in good agreement with the observed value of 27° (Burkepile et al. 2004). This agreement, which is meaningful because the apparent latitude is insensitive to the geometrical shape, suggests that this distribution of orientation angles is consistent with the observations.

Note that the coarseness of the distribution of orientation angles is apparent in Figure 4 (*bottom*), where the four peaks in the distribution reflect the four specified values of λ_0. Additional computations showed that the results were insensitive to the number of latitude angles that were included. For example, when five latitude values were used instead of the four values included above, neither the mean nor its uncertainty changed within the number of significant figures reported here. Adjustments in the range of latitudes were also considered, so as to better approximate the observed distribution of apparent latitudes; these adjustments affected the mean angular width by less than 1%.

Naturally, it is expected that the mean angular width of the synthetic image ensemble will vary with geometrical parameters

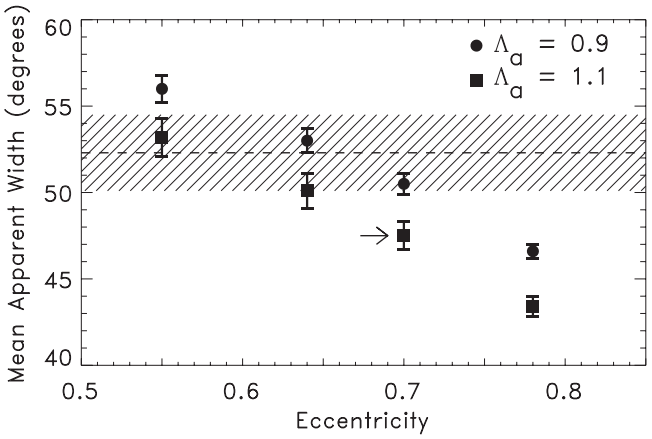

FIG. 5.—Mean angular width versus ϵ is plotted for $\Lambda_a = 0.9$ (*circles*) and $\Lambda_a = 1.1$ (*squares*). The result for $\epsilon = 0.70$ and $\Lambda_a = 1.1$ is marked with an arrow.

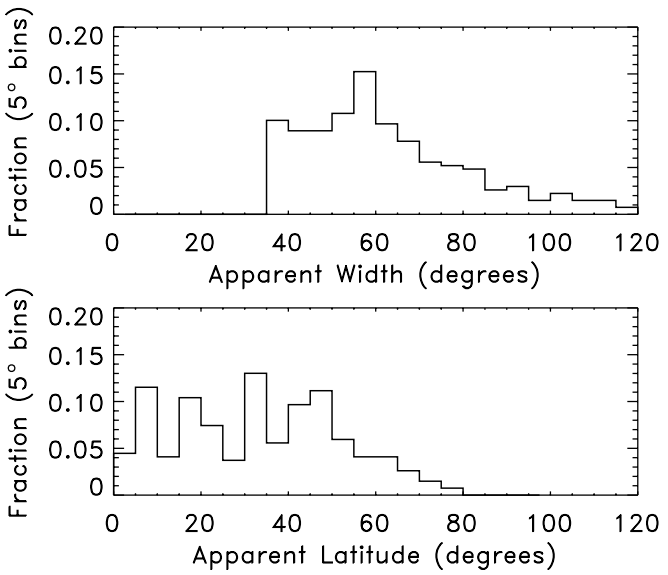

FIG. 6.—Distribution of apparent angular widths (*top*) and apparent latitudes (*bottom*) generated from a single model geometry with varying orientations and with a broad array of source locations.

ϵ and Λ_a. In Figure 5, results for the mean angular width are plotted for $\Lambda_a = 0.9$ (*circles*), $\Lambda_a = 1.1$ (*squares*), and various values of ϵ. We can see, as reported above, that the mean value for $\epsilon = 0.70$ and $\Lambda_a = 1.1$ (marked with an arrow) is 9% smaller than the *SMM* result (indicated by the dashed line, with shading for the uncertainty). It is also clear that the synthetic result can be brought into line with the *SMM* result by either reducing Λ_a to 0.9 or reducing ϵ to 0.6. While this does not provide a unique solution, and therefore does not represent a new determination of the "typical CME geometry," it does show that pairs of geometrical parameters that provide agreement with this *SMM* result are well within the range determined by Krall & St. Cyr (2006) of $\epsilon = 0.7 \pm 0.2$ and $\Lambda_a = 1.1 \pm 0.3$.

5. COMPARISON TO STATISTICAL MEASURES OF ALL *SMM* CME EVENTS

In addition to determining statistical properties of limb CMEs, Burkepile et al. (2004) also produced statistical measures of a much larger set of events, "all *SMM* CMEs," consisting of 1462 events with no restriction on source longitude. As expected from projection effects, the observed distribution of apparent latitudes for the larger set shows a greater percentage of high-latitude events than was seen in the limb-event study (see Fig. 3 of Burkepile et al. 2004). However, contrary to expectation based on the projection effect, the mean apparent angular width for the larger set of CMEs was $46.2^\circ \pm 0.6^\circ$, a value that is *smaller* than for the limb events.

This discrepancy between a simple, logical expectation (that events far from the limb should appear wider) and the observational result (the mean angular width was smaller) is discussed by Burkepile et al. (2004) in their §§ 2.3 and 3.1. If correct, one would conclude that the limb CMEs of that study were wider, on average, than a typical CME. However, the only selection criteria for limb events was that they have associated surface activity, an EP or a flare, that confirms a source location within 15° of the limb. In that same paper (see their Figs. 4 and 5) it is shown that CMEs with an EP do not differ significantly in angular width from those without an EP. A similar result is found for CMEs with/without flares.

In order to create a fuller population of synthetic CME images for comparison to the Burkepile et al. (2004) result for all *SMM* CMEs, the number of longitudes in the distribution was expanded relative to the limb-event study above. Consistent with Burkepile et al. (2004), synthetic CME images in which the angular width exceeds 120° were discarded, so there was no need to consider events close to $\phi_0 = 0$. In this case, the longitude values are $\phi_0 = 19^\circ, 28^\circ, 36^\circ, 44^\circ, 53^\circ, 61^\circ, 69^\circ, 78^\circ$, and 86°, which are evenly spaced between 15° and 90°. As above, the latitudes are $\lambda_0 = 6^\circ, 19^\circ, 31^\circ$, and 44°, which are evenly spaced between 0 and 50°, and the tilt angles are $\alpha_y = -79^\circ, -56^\circ, -34^\circ, -11^\circ, 11^\circ, 34^\circ, 56^\circ$, and 79°, which are evenly spaced within the range $90^\circ \leq \alpha_y \leq -90^\circ$. For simplicity, the angular distribution of flux ropes is again assumed to be uniform within the chosen ranges. The full set of orientation angles provides an ensemble of 288 synthetic coronagraph images, each generated with a projected leading-edge height of 4.0 $R_\odot$. Of these, 19 had an angular width in excess of 120° and were discarded.

The resulting synthetic distributions of angular widths and apparent latitudes are shown in Figure 6. The average angular width for the ensemble of 269 images is $62.3^\circ \pm 1.1^\circ$ and the median is 56°. With a larger range of longitudes, projection effects increase the rms apparent latitude from 29° to 38°, in good agreement with the 35° rms value reported by Burkepile et al. (2004).

Example synthetic coronagraph images are shown in Figure 7. Here, images correspond to all tilt angles at fixed values $\lambda_0 = 19^\circ$ and $\phi_0 = 28^\circ$. The angular widths for Figure 7 are quite large, ranging from 91.9° (Fig. 7*c*) up to 114.0° (Fig. 7*g*). In several cases it is apparent that portions of the overall CME image are extremely faint relative to narrower, brighter features. In Figure 8, four of the images from Figure 7 are again shown, but with the brightness adjusted to show the fainter details. The computed widths include these faint features, which may not be detected in an image of an actual CME with this same geometry and density structure. It is possible that the full range of CMEs captured in *SMM* images include many images similar to these, in which only one "leg" of the flux rope is detected, resulting in an apparently narrow CME. Of the 269 images in the synthetic data set, 28 had a computed width >90°; of those, 14 showed bright, narrow features combined with features that were much fainter and wider. If each such image was taken to have an angular width corresponding to the narrow, bright feature, the mean angular width of the ensemble would be reduced. This effect provides a possible explanation for the discrepancy in the *SMM* study (Burkepile et al. 2004) between the expectation based on the projection effect (that events far from

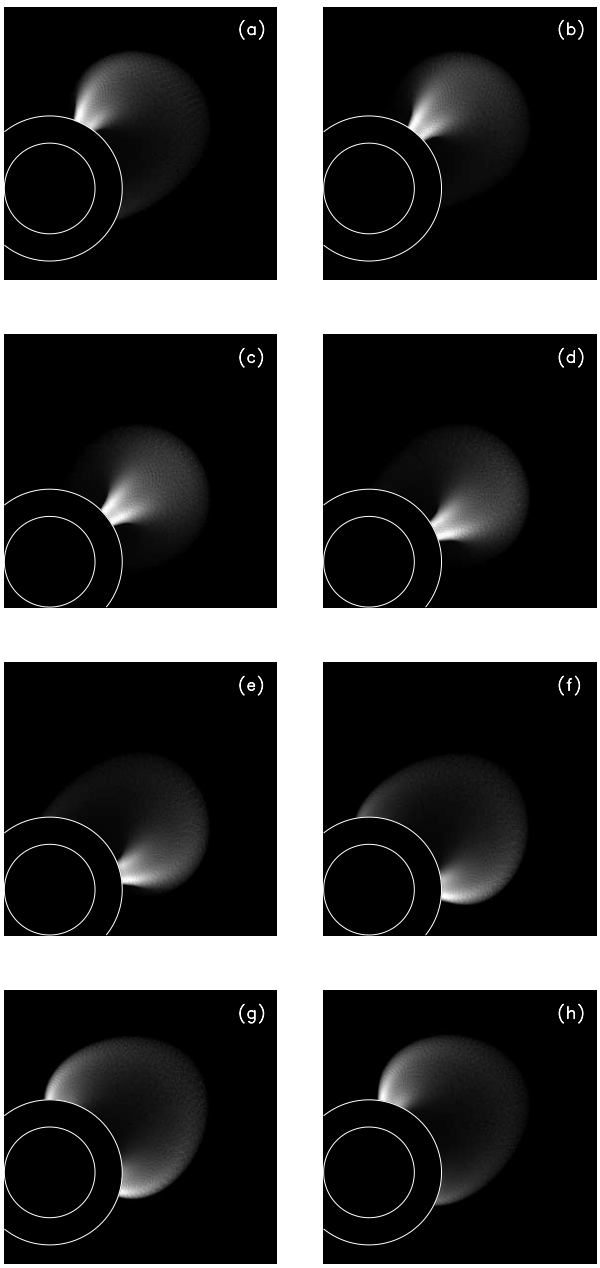

FIG. 7.—Synthetic coronagraph images corresponding to $\lambda_0 = 19^\circ$ and $\phi_0 = 28^\circ$, with (*a*) $\alpha_y = -79^\circ$, (*b*) $\alpha_y = -56^\circ$, (*c*) $\alpha_y = -34^\circ$, (*d*) $\alpha_y = -11^\circ$, (*e*) $\alpha_y = 11^\circ$, (*f*) $\alpha_y = 34^\circ$, (*g*) $\alpha_y = 56^\circ$, and (*h*) $\alpha_y = 79^\circ$. The computed angular widths for images (*a*)–(*h*) are 103.9°, 95.5°, 91.9°, 94.6°, 102.3°, 109.8°, 114.0°, and 111.0°, respectively. Their apparent latitudes are 25.5°, 29.9°, 35.8°, 42.0°, 46.8°, 45.7°, 37.4°, and 28.1°.

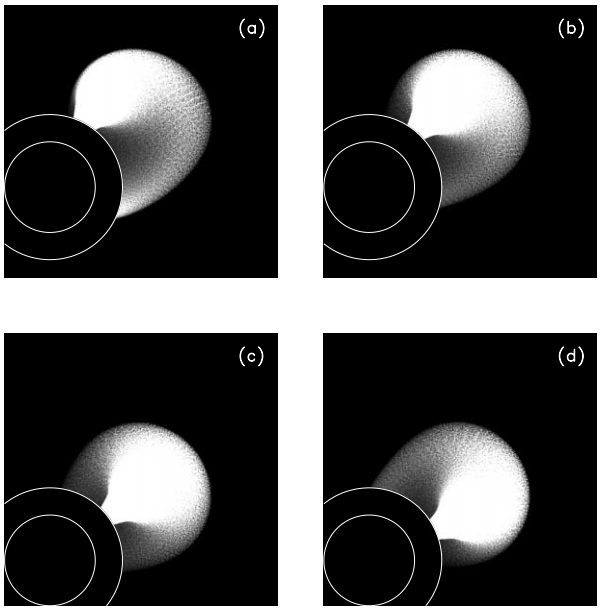

FIG. 8.—Same as Figs. 7*a*–7*d*, but with the brightness scale adjusted to better display the faintest features.

the limb should appear wider) and the result (the mean angular width of the full set of CMEs was smaller than that of the limb events).

6. COMPARISON TO THE OCCURRENCE FREQUENCY OF CONCAVE-OUTWARD FEATURES

In Webb et al. (2003), the occurrence of concave-outward features, such as that illustrated in the synthetic coronagraph image of Figure 1*a*, was reported for *SMM* CME events (see also Webb & Cliver 1995). In Webb & Cliver (1995), a concave-outward trailing feature was identified as a "candidate disconnection event" (CDE), based on an interpretation of the image in which the upper, round feature is considered to be a spherical "plasmoid" that is disconnecting from, or severing its magnetic connection to, the solar surface. Webb et al. (2003) retained this terminology, focusing on the idea that a current sheet and reconnection is likely to occur behind the apex of the three-dimensional CME structure, as represented by the CDE.

In Webb et al. (2003) and in past studies (see their references), such concave-outward features within a CME are identified as CDEs, whether or not the upper portion includes a complete circular feature. Based on these criteria, for example, images in Figure 3 (Figs. 3*c*–3*e*) and Figure 7 (Figs. 7*c* and 7*d*) can be interpreted as having CDEs. Webb et al. (2003) found that 124 out of 1182 *SMM* CMEs (10.4%) featured CDEs (see Table A1 of Webb et al. 2003). They also found that the mean angular width of CMEs associated with CDEs was 44.9° (see their Table A2).

The present study is focused on the hypothesis that virtually all such concave-outward features are flux ropes viewed nearly axially so as to highlight the minor radius near the apex. Naturally, this means that these so-called candidate disconnection events are not magnetically disconnected at all, although the field in each case must clearly decay over the course of time in order to avoid a buildup of field energy in the corona. Indeed, some erosion of the coronal field in the "legs" of a flux rope could occur during eruption without significantly altering the flux-rope hypothesis. We therefore refer to these morphological features as concave-outward features (COFs) instead of CDEs.

To proceed, the ensemble of 269 synthetic images used in § 5 above were examined, and those with concave-outward features were noted. Here, 84 (31%) of the images showed such features, and the mean angular width of the associated synthetic CMEs was 52°. The synthetic COF rate is clearly larger than the observed rate (10%), as is the mean angular width (52° versus 45° observed). It is reasonable to suppose, however, that the synthetic mean angular width is affected by cases in which the computed width includes faint features that might not be recognized in a corresponding actual coronagraph image (see discussion accompanying Fig. 8 above).

Naturally, actual CMEs and CME images are not as simply structured as those shown in the synthetic coronagraph images here. Actual CMEs often include prominence material, which is

not modeled here and which might obscure CME features of interest (COFs, in this case). Actual CME images generally include background coronal features, which also might obscure CME features. It is therefore not inconsistent with the hollow flux-rope hypothesis that the observed occurrence of COFs (10%) is less than the occurrence in the synthetic ensemble (31%). If this hypothesis were indeed correct, one might expect that the occurrence rate in images from a more sensitive coronagraph, such as LASCO, would be closer to the synthetic result. In fact, at least 23% and as many as 46% of LASCO CME events in any given calendar year show COFs (St. Cyr et al. 2000; Webb et al. 2003).

Of course, it is important to acknowledge that the identification of such features as COFs is a subjective exercise. For example, while Figure 7*c* clearly satisfies the COF morphological criteria, Figure 7*b* and Figure 7*d* might easily be included or excluded from the set of images that is said to include a COF (here, Fig. 7*d* was identified as having a COF while Fig. 7*b* was not). Nevertheless, the conclusion remains: it is possible that virtually all CMEs with COFs are in fact erupting flux ropes with the typical geometry being that of Krall & St. Cyr (2006). Finally, note that some synthetic CME images, such as Figure 3*e*, show bright, narrow radial features trailing the COF. In these synthetic images, such features occur as a result of the overlap of brightness variations resulting from the density structure within the legs of the hollow flux rope. These were identified for 8 events, or 3% of the synthetic-image ensemble.

7. CONCLUSIONS

In a recent study, Krall & St. Cyr (2006) compared an ensemble of synthetic coronagraph results based on a flux-rope geometry to a set of CME observations, with both populations of images (the synthetic coronagraph images and the actual CMEs) being filtered to discard those without a clear flux-rope morphology. In the present study, that same geometry was tested for consistency with statistical measures of general CME populations (not just those that look like flux ropes).

In this case, the CME populations come from the *SMM* catalog, as measured and described by Burkepile et al. (2004) and Webb et al. (2003). Naturally, it would be beneficial to perform a similar study using data from the LASCO coronagraph, which shows greater detail and more events relative to the *SMM* instrument. A number of observational studies have been published that might be used for this purpose, such as the St. Cyr et al. (2000) analysis of all LASCO CMEs observed through 1998 June and the catalog of 276 "structured CMEs" (and their source locations in many cases) identified by Cremades & Bothmer (2004). Because the LASCO instrument is more sensitive than the *SMM* coronagraph, the LASCO CME catalog might include classes of faint events not represented in the *SMM* catalog. Thus, the consistency that is found here between the hollow-flux-rope geometry of Krall & St. Cyr (2006) and the quantitative observational results from *SMM* (Burkepile et al. 2004; Webb et al. 2003) is not certain to be found for the LASCO CME population.

In the present study, results show that key statistical measures of CME populations can be explained in terms of an underlying hollow-flux-rope geometry as viewed with a variety orientations. In particular, the hollow-flux-rope hypothesis—that virtually all CMEs are erupting hollow flux ropes with the typical geometry being close to that determined by Krall & St. Cyr (2006)—has been shown to be in good agreement with the mean and median observed angular widths of a population of *SMM* limb CMEs (Burkepile et al. 2004; see § 4 above). The hypothesis was also shown to be consistent with the occurrence rate of concave-outward features in the general population *SMM* CME events (§ 6 above) and with the mean angular widths of CMEs associated with such events (see § 6). The hollow nature of the flux rope, with its relatively low on-axis plasma density (Chen et al. 2000; Krall & Chen 2005; Krall & St. Cyr 2006), is of key importance for the occurrence of concave-outward features, as the hollow density structure leads to these features in the synthetic coronagraph images.

In the one case where the synthetic quantitative result was in conflict with an observed quantitative result, the synthetic images provide an explanation for a confusing observation (see § 5). In particular, while the mean angular width for *SMM* limb CME events was observed to be 52°, and while projection effects should cause the mean angular width for the complete population of *SMM* CMEs to be larger than this value, the mean angular width for all *SMM* CMEs was found to be 46° (Burkepile et al. 2004). In the synthetic ensembles, the mean angular widths were 48° for limb CMEs and 62° for all CMEs, consistent with projection effects. Further, the rms apparent latitude in the synthetic image ensembles expanded from 29° for the limb events to 38° for all CMEs, consistent with the projection effect and with the observed values (27° and 35°, respectively). Examination of the synthetic images shows that a large number (one-half) of the widest events (>90°) in fact appear to be relatively narrow (the wider computed values were used in the synthetic statistical results). This effect is illustrated in Figures 7 and 8 and provides a possible explanation of the confusingly small reported value for the mean angular width of the full population of *SMM* CMEs.

In conclusion, the *SMM* results appear to be consistent with this hollow flux-rope geometry. This confirmation of the Krall & St. Cyr (2006) result should be of interest to CME modelers as they strive to obtain improved quantitative agreement between model results and corresponding observations.

This work was supported by NASA (DPR W-10106, LWS TRT Program) and the Office of Naval Research. J. Krall thanks D. F. Webb of the Air Force Research Laboratory and the Institute for Scientific Research, Boston College, for helpful discussions.

REFERENCES

Bothmer, V. 2003, in Proc. 2003 ISCS Symp., Solar Variability as an Input to the Earth's Environment, ed. A. Wilson (ESA SP-535; Noordwijk: ESA), 419
Bothmer, V., & Schwenn, R. 1994, Space Sci. Rev., 70, 215
———. 1995, J. Geomagn. Geoelectr., 47, 1127
Brueckner, G. E., et al. 1995, Sol. Phys., 162, 357
Burkepile, J. T., Hundhausen, A. J., Stanger, A. L., St. Cyr, O. C., & Seiden, J. A. 2004, J. Geophys. Res., 109, A03103, DOI: 10.1029/2003JA010149
Chen, J., et al. 1997, ApJ, 490, L191
———. 2000, ApJ, 533, 481
Cremades, H., & Bothmer, V. 2004, A&A, 422, 307
———. 2005, in IAU Symp. 226, Coronal and Stellar Mass Ejections, ed. K. P. Dere, J. Wang, & Y. Yan (Cambridge: Cambridge Univ. Press), 48
Gibson, S. E., & Low, B. C. 1998, ApJ, 493, 460
Gonzalez, W. D., Tsurutani, B. T., & Clúa de Gonzalez, A. L. 1999, Space Sci. Rev., 88, 529
Gosling, J. T. 1993, Phys. Fluids B, 5, 2638
Howard, R. A., Thernisien, A. F., Marqué, C., Vourlidas, A., & Patel, N. 2005, in Proc. Solar Wind 11/SOHO 16, Connecting Sun and Heliosphere, ed. B. Fleck, T. H. Zurbuchen, & H. Lacoste (ESA SP-592; Noordwijk: ESA), 147
Krall, J., & Chen, J. 2005, ApJ, 628, 1046
Krall, J., Chen, J., Duffin, R. T., Howard, R. A., & Thompson, B. J. 2001, ApJ, 562, 1045
Krall, J., & St. Cyr, O. C. 2006, ApJ, 652, 1740
Krall, J., Yurchyshyn, V. B., Slinker, S., Skoug, R. M., & Chen, J. 2006, ApJ, 642, 541

Marubashi, K. 2000, Adv. Space Res., 26, 55
Reif, F. 1965, Fundamentals of Statistical and Thermal Physics (New York: McGraw-Hill Book Company), 584
Rust, D. M., Anderson, B. J., Andrews, M. D., Acuña, M. H., Russell, C. T., Schuck, P. W., & Mulligan, T. 2005, ApJ, 621, 524
St. Cyr, O. C., Cremades, H., Bothmer, V., Krall, J., & Burkepile, J. T. 2004, Am. Geophys. Union 2004 Fall Meeting, Abstr. SH22A-04
St. Cyr, O. C., et al. 2000, J. Geophys. Res., 105, 18169
Strong, K. T., Saba, J. L. R., Haisch, B. M., & Schmelz, J. T., eds. 1999, The Many Faces of the Sun (New York: Springer)
Webb, D. F., Burkepile, J., Forbes, T. G., & Riley, P. 2003, J. Geophys. Res., 108, 1440, DOI: 10.1029/2003JA009923
Webb, D. F., & Cliver, E. W. 1995, J. Geophys. Res., 100, 5853
Webb, D. F., Cliver, E. W., Crooker, N. U., St. Cyr, O. C., & Thompson, B. J. 2000, J. Geophys. Res., 105, 7491
Yurchyshyn, V., Liu, C., Abramenko, V., & Krall, J. 2006, Sol. Phys., 239, 317
Yurchyshyn, V. B., Wang, H., Goode, P. R., & Deng, Y. 2001, ApJ, 563, 381